MATERIALS CHEMISTRY FRONTIERS

CCS 中国化学会 CHINESE CHEMICAL SOCIETY

ICCAS

ROYAL SOCIETY OF CHEMISTRY

RESEARCH ARTICLE

View Article Online
View Journal | View Issue

Cite this: *Mater. Chem. Front.*, 2023, **7**, 3762

Achieving high color purity in multi-resonance thermally activated delayed fluorescence emitters through a substitution-driven design strategy†

Wanlin Cai, [a] Cheng Zhong[b] and De-Yin Wu *[a]

To improve the visual quality and develop high-resolution displays, organic light-emitting diodes (OLEDs) with high color purity have garnered increasing attention. The color purity of OLEDs, which is determined by the full width at half-maximum of emission spectra, is associated with the vibronic coupling of emitters between the ground and emitting states. In this work, detailed theoretical analyses of the reorganization energy, which can characterize the strength of vibronic coupling, were conducted to clarify the color purity variations of B, O-doped polycyclic aromatic compounds with multi-resonance thermally activated delayed fluorescence (MR-TADF). The calculated results reveal that alterations in the bond length make the main contribution to the reorganization energies of these highly conjugated aromatic molecules. It is found that the origin of the large reorganization energy can be elucidated from the perspective of molecular orbitals (MOs). Moreover, the reorganization energy variations among these molecules can be rationalized by MO distribution. Based on these findings, we propose two substitution-driven design strategies to improve color purity. The first strategy involves introducing a neutral phenyl group to delocalize the orbital distribution, thereby weakening the bonding or antibonding character in frontier molecular orbitals of the bonds with a large reorganization energy. The second strategy entails the substitution at the position related to large reorganization energy with electron-donating or electron-withdrawing groups, thus decreasing the bond order difference between the MOs involved in the transition.

Received 24th March 2023,
Accepted 31st May 2023

DOI: 10.1039/d3qm00280b

rsc.li/frontiers-materials

1. Introduction

Organic light-emitting diodes (OLEDs) have attracted extensive attention from both academia and industry owing to their excellent photoelectric properties and great potential in next-generation lighting devices.[1–4] Despite numerous advantages of OLEDs, the broad emission property in most organic materials is unfavorable to high-definition displays with high color purity.[5–7] This problem has become increasingly important and deserves further exploration. The major hurdle in achieving narrow emission is the vibronic coupling between the ground (S_0) and emitting states, which is associated with the intensity of vibronic transitions (vibrational peaks) in the emission spectrum.[8–11]

Although many fluorescence molecules can show narrow emission, only 25% of excitons of these materials can be utilized, which limits their further development.[5,12] Metal complexes with theoretical 100% exciton utilization were also considered as potential molecules for achieving a small full width at half-maximum (FWHM).[13,14] However, the use of noble metal complexes increases the cost and leads to environmental contamination. As a result, it is necessary to develop OLEDs based on pure organic molecules with high exciton utilization. From this perspective, third-generation OLEDs based on thermally activated delayed fluorescence (TADF) materials with a small energy gap between the lowest singlet excited state (S_1) and the lowest triplet excited state (T_1) are suitable candidates.[3,15–17] The small energy gap can facilitate the up-conversion of triplet excitons to the S_1 state, enabling efficient triplet exciton utilization. Unfortunately, conventional donor–acceptor type TADF emitters usually show broad emission with a typical FWHM of around 70–120 nm.[5,7] This is because the small energy gap in conventional TADF emitters is achieved by minimizing the overlap between the highest occupied molecular orbital (HOMO) and the lowest unoccupied molecular orbital (LUMO). Specifically, the HOMO is located

[a] *State Key Laboratory of Physical Chemistry of Solid Surface, Collaborative Innovation Center of Chemistry for Energy Materials, and Department of Chemistry, College of Chemistry and Chemical Engineering, Xiamen University, Xiamen, 361005, P. R. China. E-mail: dywu@xmu.edu.cn*
[b] *Hubei Key Lab on Organic and Polymeric Optoelectronic Materials, Department of Chemistry, Wuhan University, Wuhan, Hubei 430072, P. R. China*

† Electronic supplementary information (ESI) available. See DOI: https://doi.org/10.1039/d3qm00280b

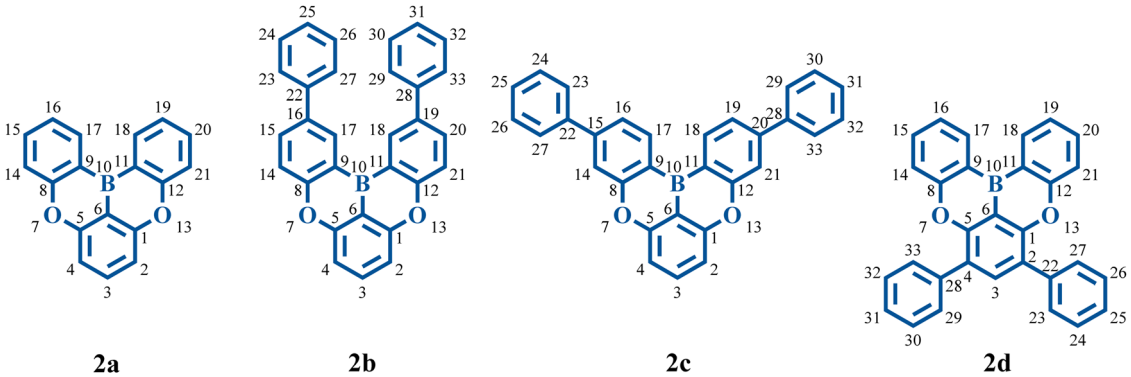

Fig. 1 Chemical structures of **2a**, **2b**, **2c**, and **2d**.

on the donor, while the LUMO is located on the acceptor. This long-distance spatial separation enhances intramolecular charge transfer and thus increases vibronic coupling.[18,19]

In 2015, Hatakeyama and colleagues proposed a solution strategy to address the broad emission problem mentioned above, named the multi-resonance TADF (MR-TADF), which presents a complementary distribution pattern of frontier molecular orbitals (FMOs) on adjacent atoms.[20] This separated FMO distribution can make MR-TADF emitters present not only a small S_1–T_1 energy gap, but also an evident nonbonding molecular orbital (MO) character.[20] This nonbonding character is associated with weak vibronic coupling between S_1 and S_0 states.[18,21–25] The synthesized B, O-doped polycyclic aromatic compounds can show a narrow FWHM of around 30 nm.[20] The molecular structures are shown in Fig. 1. It is interesting to note that introducing two phenyl rings at different positions of **2a** (with a FWHM of 34 nm experimentally) results in different variations in color purity. The FWHM of **2b** is reduced to 28 nm, while the FWHM of **2d** is enlarged to 49 nm, and there is no apparent variation in **2c** (with a FWHM of 33 nm). Since then, there has been a surge in the development of high-performance MR-TADF emitters.[22,25–31] As the landmark molecules which lay down the basic skeleton of MR-TADF emitters, the nature of FWHM variations (vibronic coupling differences) in the four molecules remains to be clarified. Exclusive reliance on molecular rigidity and π-conjugation strength is insufficient to comprehend vibronic coupling.[26] To better measure the strength of vibronic coupling, reorganization energy is commonly used.[32–37] Moreover, research shows that the bond-order-bond-length (BOBL) relationship can provide valuable insights into reorganization energy.[32,38,39]

In this work, we aim to explore the underlying nature of color purity variations among the four molecules and establish an intuitive and reliable design rule for high color purity MR-TADF emitters. First, we performed the normal mode analysis and decomposed reorganization energy into internal coordinates. Next, we carefully elucidated the intuitive BOBL relationship under the MO framework to comprehend the origin of vibronic coupling and the role of the phenyl group in modulating vibronic coupling strength. It should be noted that MO theory is a powerful tool for chemists to use their chemical intuition to analyze problems. Finally, we explored the impact

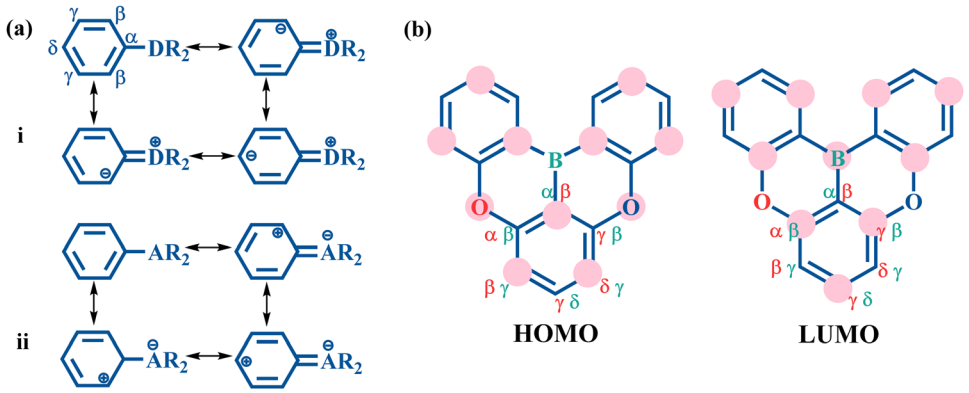

Fig. 2 (a) Resonance structures of monosubstituted benzene with the electron donating and electron deficient groups, respectively. Here, ⊕ and ⊖ denote the decrease and increase in charge distribution, respectively. (b) HOMO and LUMO distribution of molecule **2a** affected by heteroatoms. Here, the atom surrounded with a pink circle denotes an increase in distribution, while the atom surrounded without a pink circle denotes a decrease in distribution.

of substitution group electronic effects on vibronic coupling. This study can provide meaningful insights for chemists to design MR-TADF emitters.

2. Theoretical background and computational details

In the resonance representation, the electron donating group (D) increases the charge distribution at the *ortho* and *para* positions (Fig. 2a(i)). This corresponds to an increased HOMO distribution and a decreased LUMO distribution at the β and δ positions. In contrast, the electron withdrawing group (A) decreases the charge population at the *ortho* and *para* positions (Fig. 2a(ii)), which indicates a decreased HOMO distribution and an increased LUMO distribution at the β and δ positions. To illustrate the multi-resonance effect, the MR-TADF emitter **2a** serves as an example (Fig. 2b). This effect is achieved by the combination of an electron donating O atom and an electron withdrawing B atom. The multi-resonance effect decreases the HOMO distribution at the α and γ positions of the O atom and at the β and δ positions of the B atom, and increases the HOMO distribution at the β and δ positions of the O atom and at the α and γ positions of the B atom. In the meantime, the multi-resonance effect results in an opposite change behavior in the LUMO distribution at these positions. As a result, the studied MR-TADF emitters can present separated frontier orbitals.

For the studied four molecules shown in Fig. 1, the geometric optimizations and vibrational frequency calculations of S_0 and S_1 states were carried out using density functional theory (DFT) and time-dependent DFT (TDDFT), respectively, with the dispersion corrected PBE0-D3BJ functional and def2-SVP basis set.[40–43] Note that TDDFT calculations are capable of providing a good description of S_1 excitation energy.[17] All these calculations were performed using the Gaussian 16 program with the polarizable continuum model (PCM) in the solvent of CH_2Cl_2.[44–46]

Under the harmonic oscillator approximation, the reorganization energy decomposed into contributions from vibrational normal modes can be represented by

$$\lambda = \sum_k \lambda_k = \frac{1}{2}\sum_k \omega_k{}^2 \Delta Q_k{}^2 \quad (1)$$

where ω_k is the vibrational frequency and ΔQ_k is the displacement along the kth normal mode coordinate between the equilibrium positions of S_1 and S_0 states. Moreover, ΔQ_k can be expressed as linear combinations of internal coordinates (bond lengths, bond angles, and dihedral angles) to identify the contribution of molecular segments to reorganization energy, *i.e.*, $\Delta Q_k = \sum_j \alpha_{kj} \Delta R_j$, where ΔR_j is the displacement along the jth internal coordinate between the equilibrium positions of S_1 and S_0 states, and α_{kj} is the combination coefficient.[47] The vibronic coupling analyses mentioned above and emission spectra were calculated using the MOMAP program.[48]

Table 1 Calculated vertical absorption energy (ΔE_{vert}^{abs}, eV), adiabatic excitation energy (ΔE_{ad}, eV), vertical emission energy (ΔE_{vert}^{emi}, eV), HOMO–LUMO energy gap (ΔE_{L-H}, eV), oxidation–reduction energy gap ($\Delta q(E_{ox} - E_{red})$, eV), VIP–VEA energy gap ($\Delta E_{VIP-VEA}$, eV), oscillator strength (f) and full width at half-maximum (FWHM, nm)

	ΔE_{vert}^{abs}	ΔE_{ad}	ΔE_{vert}^{emi}	ΔE_{L-H}	$\Delta q(E_{ox} - E_{red})$	$\Delta E_{VIP-VEA}$	f	FWHM
2a	3.52	3.39	3.28	4.04	3.76	3.83	0.20	33
2b	3.35	3.23	3.16	3.87	3.59	3.65	0.28	27
2c	3.37	3.23	3.11	3.83	3.57	3.61	0.46	36
2d	3.26	3.10	2.94	3.64	3.41	3.39	0.13	48

3. Results and discussion

3.1 Electronic transition properties

The electronic transition properties were used as the entry point to elucidate the complicated photophysical process. Compared with **2a**, these molecules introduced with two phenyl rings (**2b**, **2c**, and **2d**) have smaller excitation energies (Table 1). The S_1 excitation energy decreases in the order of **2a** > **2b** ≈ **2c** > **2d**. For the four molecules, S_1 excitation is dominated by HOMO → LUMO transition. As shown in Fig. 3a, there is an apparent HOMO distribution on the C2, C4, C16, and C19 atoms of **2a**, and this distribution on the C2 and C4 atoms is more noticeable than that on the C16 and C19 atoms. Therefore, the increase in the HOMO level resulting from the conjugation effect of the phenyl ring is more pronounced in **2d** as compared with **2b** (Fig. 3b). On the other hand, there is no HOMO distribution but a noticeable LUMO distribution on the C15 and C20 atoms of **2c**. Therefore, the conjugation effect does not increase the HOMO level but decreases the LUMO level. On the whole, with the enlarged conjugation degree, **2b**, **2c**, and **2d** present a smaller HOMO–LUMO gap and emission energy compared with **2a**.

Additionally, we also investigated the oxidation and reduction potentials and compared the oxidation–reduction energy gap ($\Delta q(E_{ox} - E_{red})$) to the HOMO–LUMO energy gap (ΔE_{L-H}). As shown in Table 1, $\Delta q(E_{ox} - E_{red})$ has a strong linear correlation with ΔE_{L-H}. Assuming no structural relaxation and thermal correction to Gibbs free energy of the oxidation and reduction processes, the vertical ionization potential (VIP) is equal to qE_{ox} and vertical electron affinity (VEA) is equal to qE_{red}, where q is the electron charge.[49,50] According to Koopmans' theorem, VIP and VEA are approximately equal to the negative HOMO and LUMO energies, respectively.[51,52] As a result, the structural relaxation and electron correlation make the main contribution to the difference between $\Delta q(E_{ox} - E_{red})$ and $\Delta E_{LUMO-HOMO}$.

3.2 Absorption and emission spectra

We then considered absorption and emission spectra from the view of theoretical calculations and give a detailed explanation of the relationship between color purity and vibronic coupling. According to the time-dependent perturbation theory, the Fermi golden rule can be conducted to estimate the spectrum. After the Born–Oppenheimer approximation and Condon

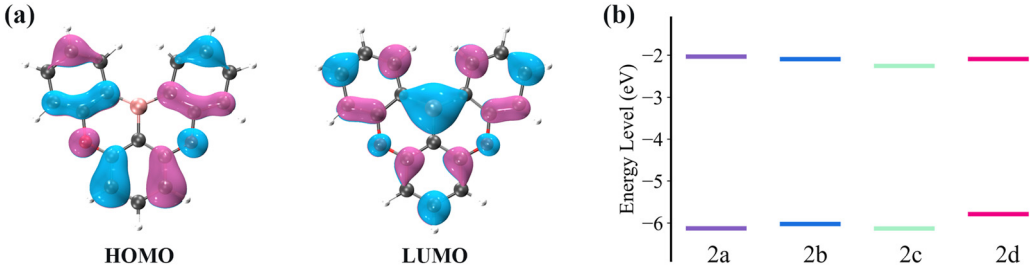

Fig. 3 (a) HOMO and LUMO distribution (isovalue = 0.03 au) of **2a**. (b) HOMO and LUMO levels for the four compounds, **2a**, **2b**, **2c**, and **2d**.

approximation, the absorption and emission spectra can be described as[53,54]

$$\alpha_{abs}(\omega, T) = \frac{4\pi^2\omega}{3\hbar c}|\mu_{fi}|^2 \sum_{v}\sum_{v'} P_{iv}|\langle \Theta_{fv'} \mid \Theta_{iv}\rangle|^2 \delta(\omega - \omega_{fv',iv}) \quad (2)$$

$$\alpha_{em}(\omega, T) = \frac{4\omega^3}{3\hbar c^3}|\mu_{fi}|^2 \sum_{v}\sum_{v'} P_{iv}|\langle \Theta_{fv'} \mid \Theta_{iv}\rangle|^2 \delta(\omega_{fv',iv} - \omega) \quad (3)$$

where μ_{fi} is the transition dipole moment; P_{iv} is the Boltzmann distribution for the initial vibronic state iv; $\omega_{fv',iv}$ is the energy difference between the initial iv and final fv' vibronic states. $|\langle \Theta_{fv'} \mid \Theta_{iv}\rangle|^2$ is the Franck–Condon factor (I_{FC}), and determines the relative intensity of vibronic peaks. I_{FC} can be evaluated as $\prod_k \frac{S_k^{v_k'}}{v_k'!} e^{-S_k}$ when $v = 0$, where S_k is the Huang–Rhys factor for the kth vibrational normal mode.[53] Moreover, $S_k = \lambda_k/\hbar\omega_k$, where λ_k is the reorganization energy used to characterize vibronic coupling strength. When the vibronic coupling is weak, the emission spectrum is dominated by the 0–0 vibronic transition, resulting in high color purity (small FWHM). In contrast, when the vibronic coupling is strong, the emission spectrum displays noticeable vibronic peaks, which broadens the spectrum and subsequently reduces color purity.[55]

Fig. 4a and b show the simulated absorption and emission spectra for the four molecules. It shows that **2b**, **2c**, and **2d** display red-shifted absorption and emission compared with **2a**. The calculated maximum absorption peaks of **2a–2d** are 374, 392, 392, and 402 nm, respectively. In the meantime, the calculated maximum emission peaks of **2a–2d** are 381, 400, 404, and 420 nm, respectively, which is close to the experimental values of 398, 410, 410, and 436 nm.[20] The emission spectra exhibit a near mirror image relationship with the absorption spectra. Since the bulk of the reorganization energy following electronic excitation arises from a stretching mode with an energy of about 1400 cm^{-1}, we use this value as an effective frequency to clarify the relationship between the

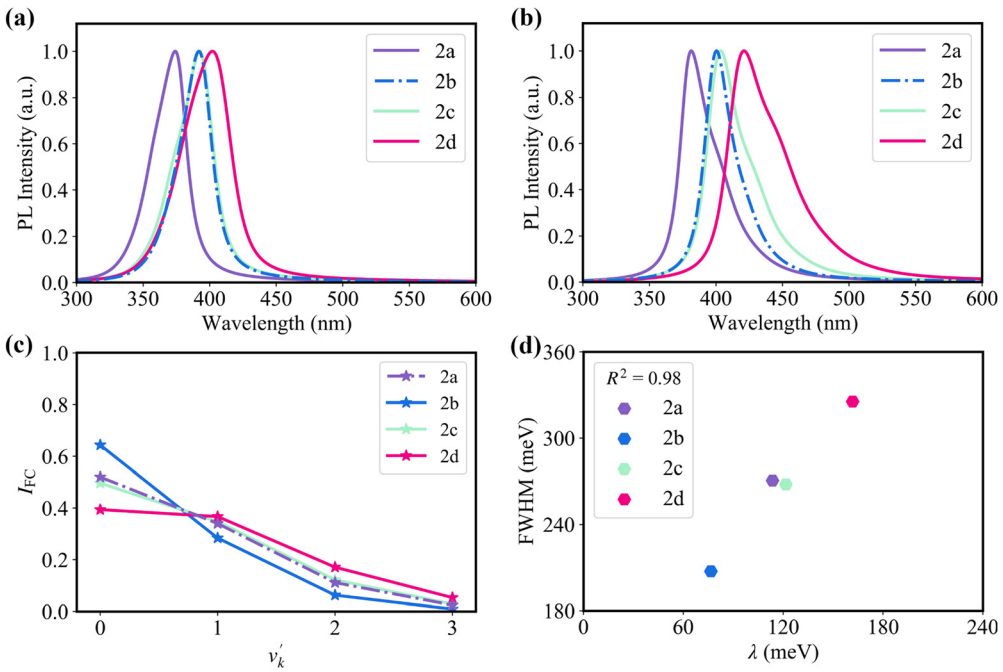

Fig. 4 (a) Calculated (a) absorption and (b) fluorescence emission spectra of **2a**, **2b**, **2c**, and **2d**. (c) The Franck–Condon factors of a 1400 cm^{-1} effective mode with varying reorganization energies among the four emitters. (d) The correlation between reorganization energy and FWHM.

Franck–Condon factor and the reorganization energy of the studied four emitters (Fig. 4c).[56] The Franck–Condon factors for the 0–ν' (from ν = 0 of S_1 to $\nu' \geq 1$ of S_0) transitions are positively proportional to the magnitude of reorganization energy. The relative intensity (I_{0-1}/I_{0-0}) of the 0–1 and 0–0 vibronic transitions increases in the order of **2b** < **2a** ≈ **2c** < **2d**. Note that the strength of 0–ν' vibronic peaks determines the FWHM of the spectrum.

Consistent with the above discussion, as shown in Fig. 4b and 4d, 2b with weak vibronic coupling (a small reorganization energy of 76.6 meV) exhibit high color purity (broad emission spectrum), while **2d** with strong vibronic coupling (a large reorganization energy of 161.7 meV) exhibits low color purity (narrow emission spectrum).[20] Here, we used a Lorentzian broadening of 900 cm^{-1} by considering environment effects to match experimental results (Fig. S7, ESI†).[57,58] The coefficient of determination (R^2) between reorganization energy and FWHM reaches 0.98 (Fig. 4d). As a consequence, to design high color purity MR-TADF emitters, we should pay attention to clarifying the nature of vibronic coupling and thus weakening it.

3.3 Analysis of the vibronic coupling between S_1 and S_0 states

Fig. 5 shows that the reorganization energies of the studied molecules mainly come from the stretching modes (alterations in bond length) within the range of 1400–1700 cm^{-1}. These normal modes with large reorganization energy make noticeable contributions to the vibronic peaks (low energy region) of emission spectra. The displacement vectors of these modes are given in Fig. S2–S5 (ESI†). In the internal coordinate representation, the reorganization energy originates from the alterations of bond lengths, bond angles, and dihedral angles. Fig. 6 shows the reorganization energy from bond length alterations (λ_{BL}), which corresponds to the aforementioned stretching modes. In particular, the C1–C2 and C4–C5 bonds in **2a** make the major contribution to λ_{BL}, with a sum of 230.9 cm^{-1} (28.6 meV). The reorganization energy variations caused by the introduction of phenyl rings for **2b** and **2d** are −37.0 and 48.1 meV, respectively. It should be noted that these variations are primarily from λ_{BL}, contributing 95% for **2b** (−35.3 meV) and 77% for **2d** (37.1 meV). Moreover, the C1–C2 and C4–C5 bonds make a large contribution to the reorganization energy variations, −21.3 meV for **2b** and 12.3 meV for **2d**.

To deeply understand the vibronic coupling, we employed the BOBL relationship under the MO framework to rationalize the magnitude of λ_{BL}. Based on the harmonic approximation, the reorganization energy in the BOBL relationship can be evaluated using the equation:[37,38]

$$\lambda_{BOBL} = \frac{1}{2}\sum_{\mu\nu\in bonds} k_{\mu\nu}\Delta R_{\mu\nu}^{\ 2} \quad (4)$$

where $k_{\mu\nu}$ is the force constant of the bond with the μth and νth atoms, $R_{\mu\nu}$ is the variation of the bond length. Under the BOBL relationship, the bond length can be calculated using $R_{\mu\nu}$ = $-0.2P_{\mu\nu}$ + 1.534, where the bond order $P_{\mu\nu} = \sum_{i=1}^{N} n_i C_\mu^i C_\nu^i$ is associated with the number of electrons in the chemical bond. Here, n_i is the occupation number of the ith molecular orbital, C_μ^i and C_ν^i are the p_z coefficients for the ith MO. For the HOMO → LUMO S_1 excitation, the bond order difference between S_1 and S_0 states is $\Delta P_{\mu\nu} = P_{\mu\nu}^{S_1} - P_{\mu\nu}^{S_0} = C_\mu^L C_\nu^L - C_\mu^H C_\nu^H$. Therefore,

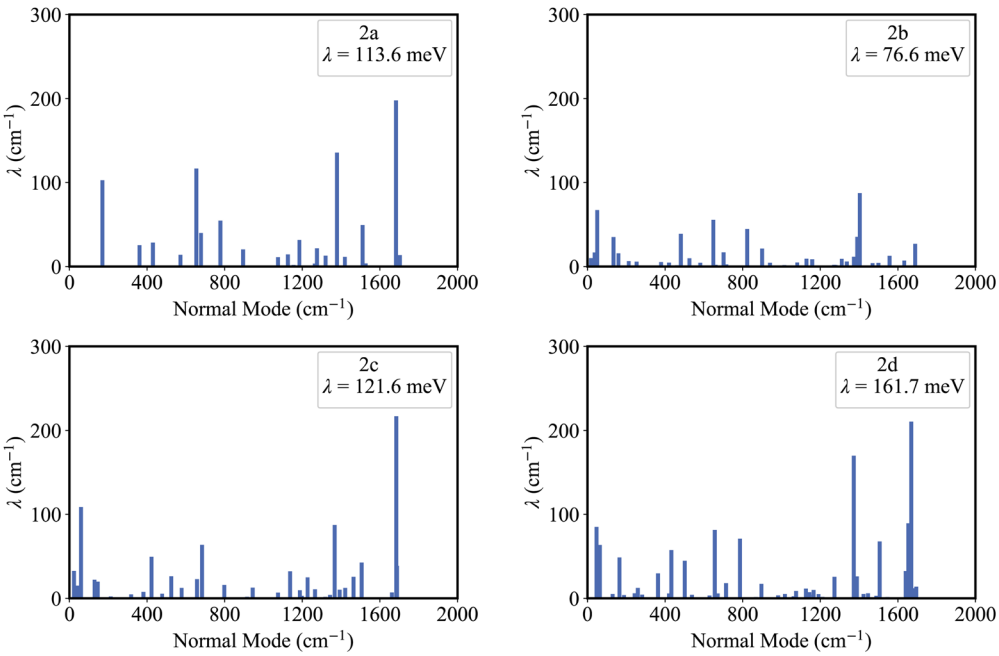

Fig. 5 The contribution of the normal modes to the reorganization energy, for **2a**, **2b**, **2c** and **2d**.

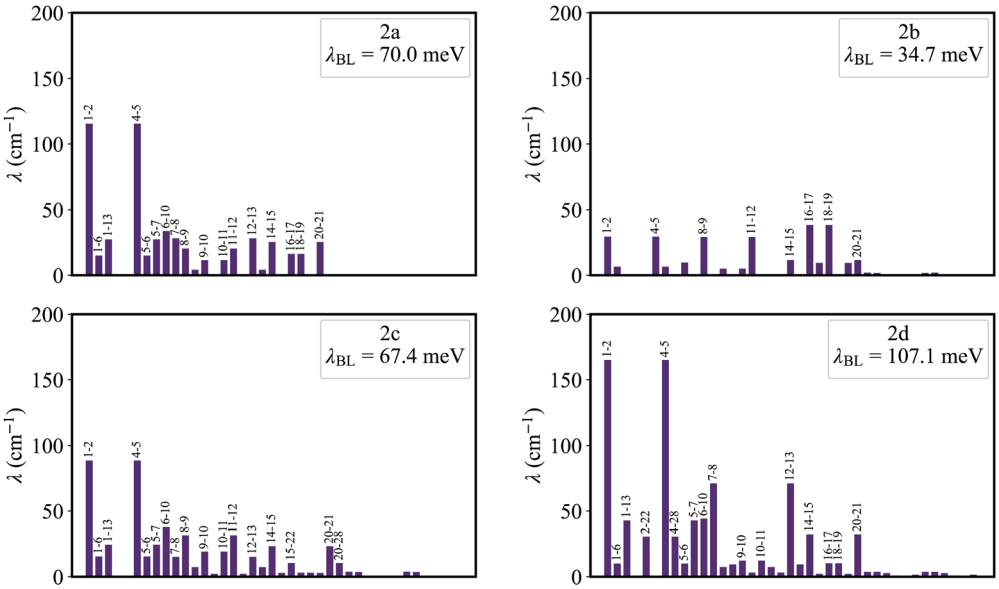

Fig. 6 The contribution of chemical bonds to λ_{BL} for **2a**, **2b**, **2c** and **2d**.

λ_{BOBL} can be estimated from $0.02\sum_{\mu\nu\in\text{bonds}} k_{\mu\nu}\left(C_\mu^L C_\nu^L - C_\mu^H C_\nu^H\right)^2$. In this work, we refer to $C_\mu^H C_\nu^H$ and $C_\mu^L C_\nu^L$ as the HOMO and LUMO bond orders, respectively, reflecting their contribution to $P_{\mu\nu}$. The general form for multi-MO transition excitation is

$$\lambda_{BOBL} = 0.02\sum_{ia\in n} {c_{n,ia}}^2 \sum_{\mu\nu\in\text{bonds}} k_{\mu\nu}\left[\left(C_\mu^i C_\nu^i\right)^2 + \left(C_\mu^a C_\nu^a\right)^2 - 2C_\mu^i C_\nu^i C_\mu^a C_\nu^a\right] \quad (5)$$

where $c_{n,ia}$ is the configuration interaction coefficient between the ith and ath molecular orbitals in TDDFT. λ_{BOBL} is associated with two parameters, η and ϕ, which are respectively defined as[37]

$$\eta = \sum_{ia\in n} {c_{n,ia}}^2 \sum_{\mu\nu\in\text{bonds}} \left[\left(C_\mu^i C_\nu^i\right)^2 + \left(C_\mu^a C_\nu^a\right)^2\right] \quad (6)$$

$$\phi = -\sum_{ia\in n} {c_{n,ia}}^2 \sum_{\mu\nu\in\text{bonds}} C_\mu^i C_\nu^i C_\mu^a C_\nu^a \quad (7)$$

Accordingly, λ_{BOBL} is proportional to parameter $\kappa(\lambda_{BOBL} \propto \kappa)$, which is

$$\kappa = \eta + 2\phi \quad (8)$$

where κ is associated with the bond order difference. η is determined by the electron densities of bonded atoms, while ϕ is related to the transition density. For conventional TADF emitters, if they do not exhibit the nonbonding character as MR-TADF emitters, the localized HOMO and LUMO distributions may result in a noticeable HOMO–LUMO bond order difference (a large κ) in both the donor and the acceptor (Table S3, ESI†). Moreover, this large κ (large reorganization energy) can be responsible for the broad emission in conventional TADF emitters. The code for the calculation of κ is available at **https://github.com/Wanlin-Cai/BOBL**.

Fig. 7 plots the contribution of chemical bonds to κ in the four molecules. Taking **2a** as an example, the C1–C2 and C4–C5 bonds present the largest value of κ in **2a**, which indicates that the two bonds have large reorganization energy from the view of MO. This significant κ of the C1–C2 and C4–C5 bonds is an important source of the vibronic peaks in the emission spectrum. Here, this significant κ (associated with the bond order difference) can be attributed to the different distribution behavior of transition orbitals. The C1–C2 and C4–C5 bonds of **2a** in the LUMO show the nonbonding character (Fig. 3a). However, due to the orbital antisymmetry of the HOMO, there is no HOMO distribution at the B atom, which means that the B atom cannot present efficient resonance character (decreasing the HOMO distribution at the β and δ positions and increasing the HOMO distribution at the α and γ position). Therefore, the two bonds in the HOMO show a noticeable bonding character. Moreover, based on the strong bonding character in the HOMO and the nonbonding character in the LUMO, the C1–C2 and C4–C5 bonds present large κ and reorganization energy.

3.4 Vibronic coupling variations caused by phenyl ring substitution

As shown in Fig. 3a, there is an evident HOMO distribution on the C16 and C19 atoms. Due to the conjugation effect of the phenyl group, the introduction of a phenyl ring to the C16 and C19 atoms (**2b**) gives rise to the delocalization in the HOMO, as evidenced by the HOMO distribution observed on the attached phenyl rings (Fig. S1, ESI†). This delocalized behavior is also reflected in the reduction of the HOMO distribution on the C1, C2, C4, and C5 atoms (Fig. 8). This reduction in the four atoms signifies a weakened bonding character of the C1–C2 and C4–C5 bonds in the HOMO, which further implies a weakened

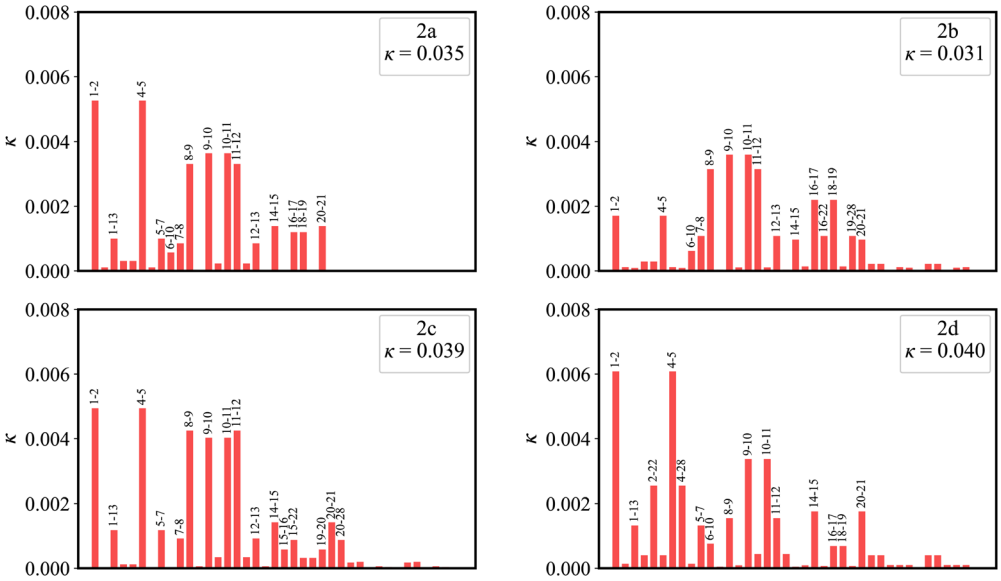

Fig. 7 The contribution of chemical bonds to κ for **2a**, **2b**, **2c** and **2d**.

HOMO–LUMO bond order difference (associated with κ) of the two bonds in **2b**. On the other hand, there is a noticeable LUMO distribution on the C15 and C20 atoms in **2a** (Fig. 3a). The introduction of a phenyl ring to the C15 and C20 atoms (**2c**) reduces the LUMO distribution on the C1, C2, C4, and C5 atoms for the conjugation effect of the phenyl group. Note that there is a nearly nonbonding character of the C1–C2 and C4–C5 bonds in the LUMO. This decreased LUMO distribution on the C1, C2, C4, and C5 atoms in **2c** does not affect the HOMO–LUMO bond order difference (associated with κ). As a result, **2b** with a small κ shows a narrower emission spectrum (higher color purity) than **2a**, while **2c** shows the same FWHM (same color purity) as **2a**.

In the meantime, there is a noticeable HOMO distribution but no LUMO distribution on the C2 and C4 atoms in **2a** (Fig. 3a). Upon the introduction of a phenyl ring to the C2 and C4 atoms (**2d**), the resonance effect of the phenyl group reduces the HOMO distribution on the C2 and C4 atoms while increasing it on the C1 and C5 atoms (Fig. 8). This results in a strengthened bonding character of the C1–C2 and C4–C5 bonds in the HOMO, indicating an increased HOMO–LUMO bond order difference (associated with κ) of the C1–C2 and C4–C5 bonds in **2d**. Note that the newly introduced phenyl rings display an evident HOMO distribution, but no LUMO distribution is observed (Fig. S1, ESI†). The C2–C22 and C4–C28 bonds present the antibonding and nonbonding character in the HOMO and LUMO, respectively. This results in an evident bond order difference (associated with κ) of the C2–C22 and C4–C28 bonds. As a whole, due to the large κ of the C1–C2, C2–C22, C4–C5, and C4–C28 bonds, **2d** with strong vibronic coupling exhibits a broader emission spectrum (lower color purity) compared with **2a**.

From the discussion above, it is clear that we can weaken the vibronic coupling by delocalizing the MO distribution, thus

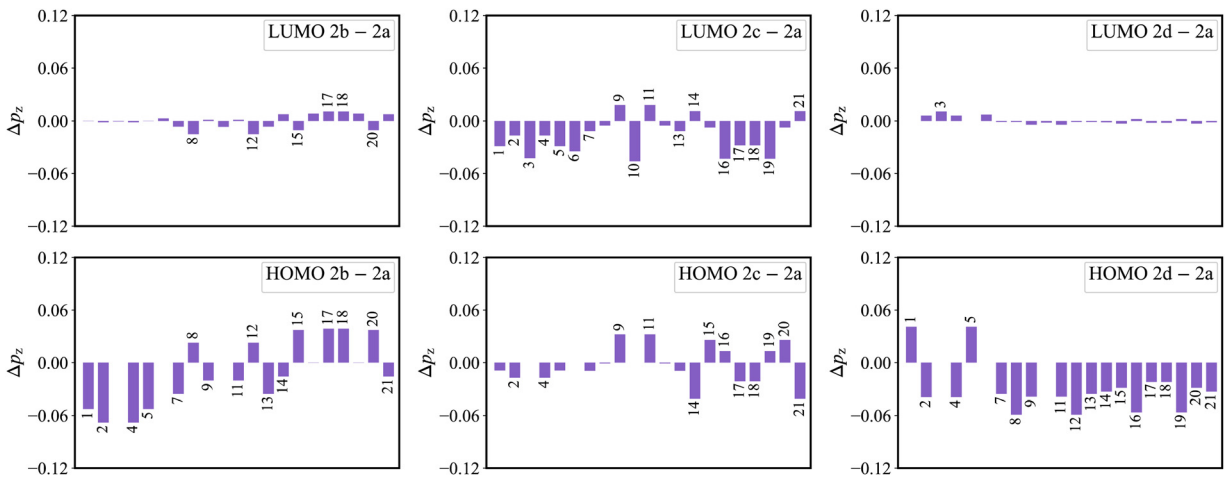

Fig. 8 The variation of p_z(**2b**/**2c**/**2d**_**2a**) on atoms.

decreasing the HOMO–LUMO bond order difference (associated with κ) of the bonds with a large reorganization energy.

3.5 Impact of substitution group electronic effects on vibronic coupling

To gain a deeper understanding of the impact of the electronic structure on vibronic coupling, we replaced the phenyl groups of **2b** and **2d** with various substituents. The selection of specific positions for substitution was driven by the observation that the substitution of phenyl rings on the C16/C19 (**2b**) and C2/C4 (**2d**) atoms significantly affects the vibronic coupling. Specifically, the substituents comprised electron-donating groups (**D1**: methoxy-substituted phenyl group, **D2**: pyrrolyl group, and **D3**: imidazolyl group) and electron-withdrawing groups (**A1**: trifluoromethyl-substituted phenyl group, **A2**: pyridyl group, and **A3**: pyrimidyl group) (Fig. 9). It is worth noting that the pyrrolyl group has a stronger electron-donating ability than the imidazolyl group, while the pyridyl group demonstrates a weaker electron-withdrawing ability compared with the pyrimidyl group.

Since the C2, C4, C16, and C19 atoms of **2a** present a noticeable HOMO distribution but no LUMO distribution (Fig. 3a), the substitution of the electron-donating groups and the electron-withdrawing groups can increase and decrease the HOMO level, respectively, while all of these substituent groups have a negligible impact on the LUMO level (Fig. 10a and b). As the orbital interaction strength is associated with the energy level difference of the two orbitals, the interaction between the HOMO of **D1**/**D2**/**D3** and the HOMO of **2a** is stronger than that between the LUMO of **A1**/**A2**/**A3** and the HOMO of **2a**. Consequently, **2b-D** series (**2b-D1**, **2b-D2**, and **2b-D2**) and **2d-D** series (**2d-D1**, **2d-D2**, and **2d-D2**) display significant red-shifted emission. In contrast, the **2b-A** series (**2b-A1**, **2b-A2**, and **2b-A2**) and **2d-A** series (**2d-A1**, **2d-A2**, and **2d-A2**) exhibit slight blue-shifted emission relative to **2b** and **2d**, respectively (Fig. 10e and f).

As shown in Fig. 10c and d, the majority of the **2b-D** and **2b-A** series of emitters present a larger reorganization energy compared with **2b**. Meanwhile, a clear trend is observed as the reorganization energy decreases in the order of **2d-D** series > **2d** > **2d-A** series. The coefficient of determination (R^2) between reorganization energy and FWHM of the fourth emitters can reach 0.99 (Fig. S22, ESI†). The FWHM values of **2b**, **2b-D** series, and **2b-A** series were calculated to be 207, 237, 289, 249, 212, 217, and 203 meV, respectively. The FWHM values of the **2d**, **2d-D** series and **2d-A** series were calculated to be 325, 348, 351, 352, 291, 261, and 237 meV, respectively.

For the **2b-D** series, the electron-donating groups significantly decrease the HOMO distribution on the C1, C2, C4, and C5 atoms (Fig. S18, ESI†), thus decreasing the HOMO–LUMO bond order difference (due to the smaller HOMO bond order) and reorganization energy of the C1–C2 and C4–C5 bonds (Fig. S14, ESI†). However, the strong electron-donating ability of these groups gives rise to an aggravated HOMO distribution in the newly introduced electron-donating groups (Fig. S10, ESI†), resulting in a large HOMO–LUMO bond order difference and reorganization energy of the bonds of the newly introduced groups (Fig. S14, ESI†). Overall, the strong electron-donating ability increase the reorganization energy. Similarly, the bonds of the newly introduced electron-donating groups in the **2d-D** series present noticeable reorganization energy (Fig. S15, ESI†), which makes the main contribution to the increase in reorganization energy from the **2d** to **2d-D** series.

It should be noted that the strength of orbital interactions decreases as the orbital levels move farther apart. In the case of the **2b-A** series, the electron-withdrawing groups with lower HOMO levels present weaker conjugation ability to decrease the HOMO distribution on the C1, C2, C4, and C5 atoms compared with the phenyl groups of **2b** (Fig. 8 and Fig. S19, ESI†). Consequently, this results in a larger HOMO–LUMO bond order difference (due to the larger HOMO bond order) and reorganization energy of the C1–C2 and C4–C5 bonds in the **2b-A** series compared with **2b** (Fig. 6 and Fig. S14, ESI†). In contrast, for the **2d-A** series, the electron-withdrawing groups have a weaker resonance effect to enhance the HOMO bond order compared with the phenyl group of **2d**. Simultaneously, the electron-withdrawing group increases the LUMO distribution on the C2 and C4 atoms (Fig. S21, ESI†), thus increasing the LUMO bond order. Consequently, the **2d-A** series present a smaller HOMO–LUMO bond order difference (due to the smaller HOMO bond order and the larger LUMO bond order) and reorganization energy of the C1–C2 and C4–C5 bonds compared with **2d**.

From the discussion above, to decrease the reorganization energy associated with the strong bonding character in the HOMO, we can substitute the position related to large reorganization energy with an electron-withdrawing group. This substitution can weaken the HOMO bonding character and

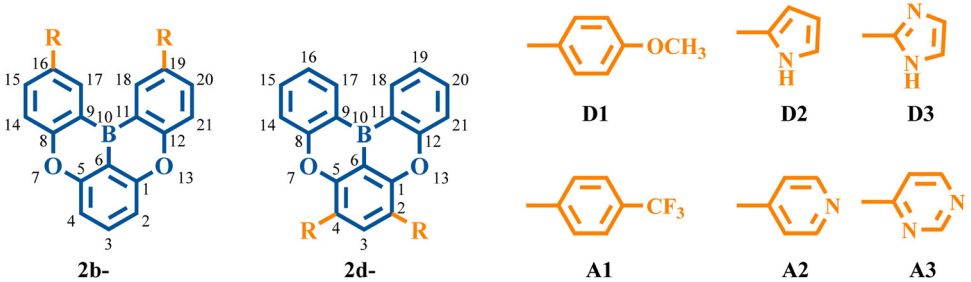

Fig. 9 Chemical structures of **2b** series and **2d** series with different electron-donating and electron-withdrawing substituents.

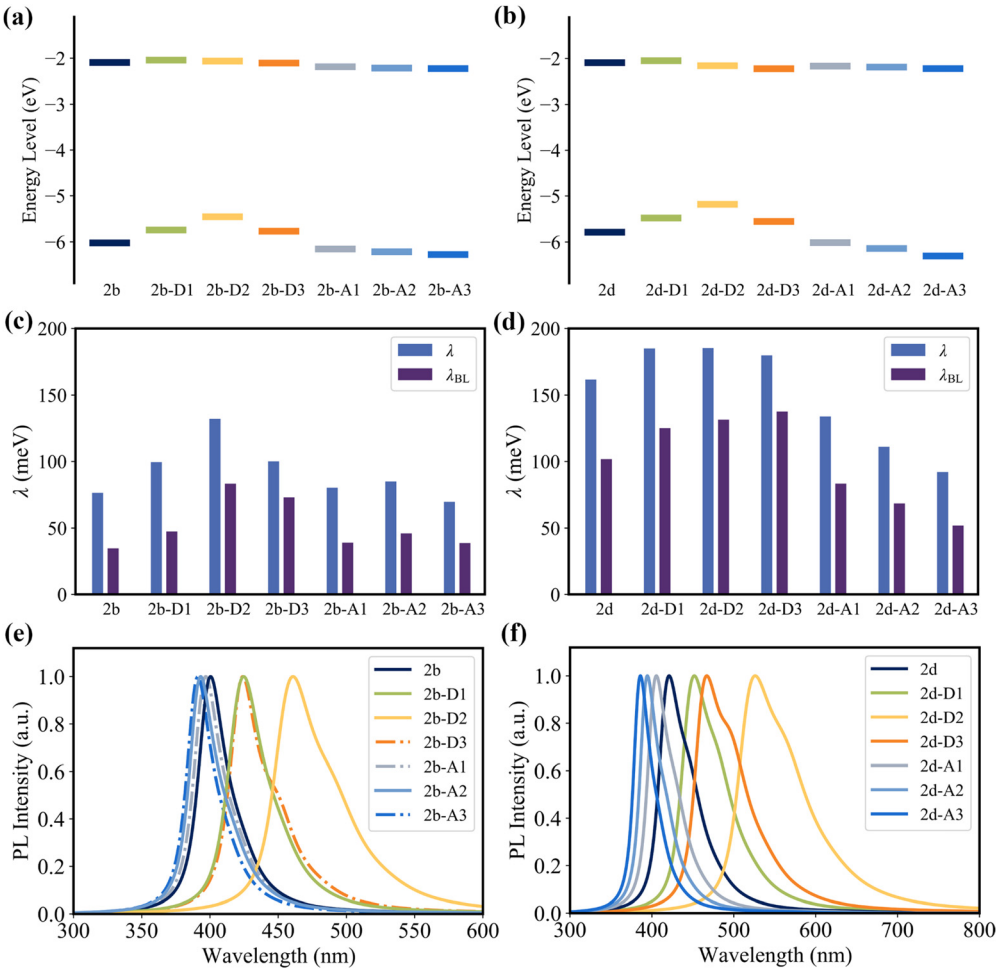

Fig. 10 HOMO and LUMO levels of (a) **2b**, **2b-D** series, and **2b-A** series and (b) **2d**, **2d-D** series, and **2d-A** series. The reorganization energy (λ) and the reorganization energy from bond length alterations (λ_{BL}) for (c) **2b**, **2b-D** series, and **2b-A** series and (d) **2d**, **2d-D** series, and **2d-A** series. Fluorescence emission spectra of (e) **2b**, **2b-D** series, and **2b-A** series and (f) **2d**, **2d-D** series, and **2d-A** series.

enhance the LUMO bonding character, thereby decreasing the HOMO–LUMO bond order difference.

4. Conclusion

In this work, a series of theoretical analyses of the reorganization energy (the vibronic coupling) were studied to elucidate the color purity of four MR-TADF emitters. It is found that bond length alterations provide the dominant contribution to the reorganization energy variations from **2a** to **2b** and **2d**, where the C1–C2 and C4–C5 bonds make a large contribution to the reorganization energy variations. Here, the large reorganization energy of the two bonds can be interpreted as the noticeable κ (associated with the HOMO–LUMO bond order difference), which can be further attributed to the strong bonding character in the HOMO.

We confirmed that it is feasible to rationalize the reorganization energy variations under the MO framework. In the case of **2b**, the conjugation effect of the phenyl group weakens the HOMO bonding character of the C1–C2 and C4–C5 bonds, leading to a decrease in the reorganization energy. Therefore, **2b** shows a narrower emission spectrum (higher color purity) compared with **2a**. In contrast, the HOMO bonding character of the two bonds in **2d** is strengthened by the resonance effect of the phenyl group, which makes a large contribution to the increase in the reorganization energy. This results in the broad emission spectrum (low color purity) of **2d**. It should be noted that the strong electron-donating ability of the **2b-D** series and **2d-D** series can give rise to the aggravated HOMO distribution on the newly introduced electron-donating groups, thus increasing the reorganization energy of the bonds of the newly introduced electron-donating groups. In the case of the **2b-A** series, the electron-withdrawing groups present a weaker ability to decrease the HOMO bonding character of the two bonds compared with the phenyl groups of **2b**. For the **2d-A** series, the substitution of the electron-withdrawing group weakens the HOMO bonding character and enhances the LUMO bonding character of the two bonds, which results in a small HOMO–LUMO bond order difference and reorganization energy. This also offers potential to improve the color purity.

For the design of MR-TADF emitters with high color purity, in addition to using the resonance effect to enhance the nonbonding character, two substitution-driven design strategies can be employed. The first strategy involves introducing a neutral phenyl group to delocalize the orbital distribution, thereby weakening the bonding or antibonding character in frontier molecular orbitals of the bonds with a large reorganization energy. The second strategy entails substitution at the position related to a large reorganization energy with electron-donating or electron-withdrawing groups, thus decreasing the HOMO–LUMO bond order difference.

Conflicts of interest

The authors declare no conflicts of interest.

Acknowledgements

This work is supported by the National Natural Science Foundation of China (22032004, 22021001, and 21533006).

References

1 H. Yersin, A. F. Rausch, R. Czerwieniec, T. Hofbeck and T. Fischer, The triplet state of organo-transition metal compounds. Triplet harvesting and singlet harvesting for efficient OLEDs, *Coord. Chem. Rev.*, 2011, **255**, 2622–2652.
2 P. K. Samanta, D. Kim, V. Coropceanu and J.-L. Brédas, Up-conversion intersystem crossing rates in organic emitters for thermally activated delayed fluorescence: impact of the nature of singlet vs triplet excited states, *J. Am. Chem. Soc.*, 2017, **139**, 4042–4051.
3 Z. Y. Yang, Z. Mao, Z. L. Xie, Y. Zhang, S. W. Liu, J. Zhao, J. Xu, Z. G. Chi and M. P. Aldred, Recent advances in organic thermally activated delayed fluorescence materials, *Chem. Soc. Rev.*, 2017, **46**, 915–1016.
4 Z. G. Shuai and Q. Peng, Organic light-emitting diodes: theoretical understanding of highly efficient materials and development of computational methodology, *Natl. Sci. Rev.*, 2017, **4**, 224–239.
5 J. M. Ha, S. H. Hur, A. Pathak, J.-E. Jeong and H. Y. Woo, Recent advances in organic luminescent materials with narrowband emission, *NPG Asia Mater.*, 2021, **13**, 1–36.
6 J.-M. Teng, Y.-F. Wang and C.-F. Chen, Recent progress of narrowband TADF emitters and their applications in OLEDs, *J. Mater. Chem. C*, 2020, **8**, 11340–11353.
7 V. V. Patil, H. L. Lee, I. Kim, K. H. Lee, W. J. Chung, J. Kim, S. Park, H. Choi, W. J. Son and S. O. Jeon, Purely spin-vibronic coupling assisted triplet to singlet up-conversion for real deep blue organic light-emitting diodes with over 20% efficiency and y color coordinate of 0.05, *Adv. Sci.*, 2021, **8**, 2101137.
8 W. L. Cai, H. Z. Zhang, X. Yan, A. C. Zhao, R. X. He, M. Li, Q. X. Meng and W. Shen, What accounts for the color purity of tetradentate Pt complexes? A computational analysis, *Phys. Chem. Chem. Phys.*, 2019, **21**, 8073–8080.
9 C. Adamo and D. Jacquemin, The calculations of excited-state properties with Time-Dependent Density Functional Theory, *Chem. Soc. Rev.*, 2013, **42**, 845–856.
10 D. Jacquemin, E. Brémond, I. Ciofini and C. Adamo, Impact of vibronic couplings on perceived colors: two anthraquinones as a working example, *J. Phys. Chem. Lett.*, 2012, **3**, 468–471.
11 S. A. Ahmad, J. Eng and T. J. Penfold, Rapid predictions of the colour purity of luminescent organic molecules, *J. Mater. Chem. C*, 2022, **10**, 4785–4794.
12 S. Y. Byeon, D. R. Lee, K. S. Yook and J. Y. Lee, Recent progress of singlet-exciton-harvesting fluorescent organic light-emitting diodes by energy transfer processes, *Adv. Mater.*, 2019, **31**, 1803714.
13 G. S. M. Tong, K. T. Chan, X. Chang and C.-M. Che, Theoretical studies on the photophysical properties of luminescent pincer gold (III) arylacetylide complexes: the role of π-conjugation at the C-deprotonated [C^N^C] ligand, *Chem. Sci.*, 2015, **6**, 3026–3037.
14 G. Baryshnikov, B. Minaev and H. Ågren, Theory and calculation of the phosphorescence phenomenon, *Chem. Rev.*, 2017, **117**, 6500–6537.
15 X.-K. Chen, D. Kim and J.-L. Brédas, Thermally activated delayed fluorescence (TADF) path toward efficient electroluminescence in purely organic materials: molecular level insight, *Acc. Chem. Res.*, 2018, **51**, 2215–2224.
16 R. Gómez-Bombarelli, J. Aguilera-Iparraguirre, T. D. Hirzel, D. Duvenaud, D. Maclaurin, M. A. Blood-Forsythe, H. S. Chae, M. Einzinger, D.-G. Ha and T. Wu, *et al.*, Design of efficient molecular organic light-emitting diodes by a high-throughput virtual screening and experimental approach, *Nat. Mater.*, 2016, **15**, 1120–1127.
17 S. Y. Lin, Q. Ou and Z. G. Shuai, Computational selection of thermally activated delayed fluorescence (TADF) molecules with promising electrically pumped lasing property, *ACS Mater. Lett.*, 2022, **4**, 487–496.
18 S. Madayanad Suresh, D. Hall, D. Beljonne, Y. Olivier and E. Zysman-Colman, Multiresonant thermally activated delayed fluorescence emitters based on heteroatom-doped nanographenes: recent advances and prospects for organic light-emitting diodes, *Adv. Funct. Mater.*, 2020, **30**, 1908677.
19 A. Pershin, D. Hall, V. Lemaur, J.-C. Sancho-Garcia, L. Muccioli, E. Zysman-Colman, D. Beljonne and Y. Olivier, Highly emissive excitons with reduced exchange energy in thermally activated delayed fluorescent molecules, *Nat. Commun.*, 2019, **10**, 597.
20 H. Hirai, K. Nakajima, S. Nakatsuka, K. Shiren, J. Ni, S. Nomura, T. Ikuta and T. Hatakeyama, One-step borylation of 1, 3-diaryloxybenzenes towards efficient materials for organic light-emitting diodes, *Angew. Chem., Int. Ed.*, 2015, **54**, 13581–13585.
21 Y.-C. Chang and I. Chao, An important key to design molecules with small internal reorganization energy: strong nonbonding character in frontier orbitals, *J. Phys. Chem. Lett.*, 2010, **1**, 116–121.

22 T. Hatakeyama, K. Shiren, K. Nakajima, S. Nomura, S. Nakatsuka, K. Kinoshita, J. Ni, Y. Ono and T. Ikuta, Ultrapure blue thermally activated delayed fluorescence molecules: efficient HOMO–LUMO separation by the multiple resonance effect, *Adv. Mater.*, 2016, **28**, 2777–2781.
23 S. M. Pratik, V. Coropceanu and J.-L. Brédas, Purely organic emitters for multiresonant thermally activated delay fluorescence: design of highly efficient sulfur and selenium derivatives, *ACS Mater. Lett.*, 2022, **4**, 440–447.
24 Z. Pei, Q. Ou, Y. Z. Mao, J. Yang, A. l d l Lande, F. Plasser, W. Z. Liang, Z. G. Shuai and Y. H. Shao, Elucidating the electronic structure of a delayed fluorescence emitter via orbital interactions, excitation energy components, charge-transfer numbers, and vibrational reorganization energies, *J. Phys. Chem. Lett.*, 2021, **12**, 2712–2720.
25 D. Hall, K. Stavrou, E. Duda, A. Danos, S. Bagnich, S. Warriner, A. M. Slawin, D. Beljonne, A. Köhler and A. Monkman, Diindolocarbazole–achieving multiresonant thermally activated delayed fluorescence without the need for acceptor units, *Mater. Horiz.*, 2022, **9**, 1068–1080.
26 Y. W. Zhang, D. D. Zhang, J. B. Wei, Z. Y. Liu, Y. Lu and L. Duan, Multi-resonance induced thermally activated delayed fluorophores for narrowband green OLEDs, *Angew. Chem., Int. Ed.*, 2019, **58**, 16912–16917.
27 Y. C. Xu, C. L. Li, Z. Q. Li, Q. Y. Wang, X. L. Cai, J. B. Wei and Y. Wang, Constructing charge-transfer excited states based on frontier molecular orbital engineering: narrowband green electroluminescence with high color purity and efficiency, *Angew. Chem., Int. Ed.*, 2020, **59**, 17442–17446.
28 S. Oda, B. Kawakami, R. Kawasumi, R. Okita and T. Hatakeyama, Multiple resonance effect-induced sky-blue thermally activated delayed fluorescence with a narrow emission band, *Org. Lett.*, 2019, **21**, 9311–9314.
29 Y. Yuan, X. Tang, X. Y. Du, Y. Hu, Y. J. Yu, Z. Q. Jiang, L. S. Liao and S. T. Lee, The design of fused amine/carbonyl system for efficient thermally activated delayed fluorescence: novel multiple resonance core and electron acceptor, *Adv. Opt. Mater.*, 2019, **7**, 1801536.
30 D. M. Sun, S. M. Suresh, D. Hall, M. Zhang, C. F. Si, D. B. Cordes, A. M. Slawin, Y. Olivier, X. H. Zhang and E. Zysman-Colman, The design of an extended multiple resonance TADF emitter based on a polycyclic amine/carbonyl system, *Mater. Chem. Front.*, 2020, **4**, 2018–2022.
31 Y. W. Zhang, G. M. Li, L. Wang, T. Y. Huang, J. B. Wei, G. Y. Meng, X. Wang, X. Zeng, D. D. Zhang and L. Duan, Fusion of Multi-Resonance Fragment with Conventional Polycyclic Aromatic Hydrocarbon for Nearly BT. 2020 Green Emission, *Angew. Chem., Int. Ed.*, 2022, **134**, e202202380.
32 W.-C. Chen and Y.-C. Chang, Rational design of organic semiconductors with low internal reorganization energies for hole and electron transport: position effect of aza-substitution in phenalenyl derivatives, *Phys. Chem. Chem. Phys.*, 2021, **23**, 18163–18172.
33 W. C. Huang, W. J. Xie, H. J. Huang, H. Zhang and H. G. Liu, Designing organic semiconductors with ultrasmall reorganization energies: insights from molecular symmetry, aromaticity and energy gap, *J. Phys. Chem. Lett.*, 2020, **11**, 4548–4553.
34 X. Zeng, X. Wang, Y. W. Zhang, G. Y. Meng, J. B. Wei, Z. Y. Liu, X. Q. Jia, G. M. Li, L. Duan and D. D. Zhang, Nitrogen-Embedded Multi-Resonance Heteroaromatics with Prolonged Homogeneous Hexatomic Rings, *Angew. Chem., Int. Ed.*, 2022, **134**, e202117181.
35 C.-C. Wu, E. Y. Li and P.-T. Chou, Reducing the internal reorganization energy via symmetry controlled π-electron delocalization, *Chem. Sci.*, 2022, **13**, 7181–7189.
36 J.-W. Huang, Y.-C. Hsu, X. Wu, S. Wang, X.-Q. Gan, W.-Q. Zheng, H. Zhang, Y.-Z. Gong, W.-Y. Hung and P.-T. Chou, Influence of charge transfer strength on emission bandwidth for multiple-resonance emitters via systematically tuning the acceptor–donor assembly, *J. Mater. Chem. C*, 2022, **10**, 7866–7874.
37 W.-C. Chen and Y.-C. Cheng, Elucidating the magnitude of internal reorganization energy of molecular excited states from the perspective of transition density, *J. Phys. Chem. A*, 2020, **124**, 7644–7657.
38 S. Larsson, A. Klimkāns, L. Rodriguez-Monge and G. Duškesas, Reorganization energies in organic π systems, *J. Mol. Struct. THEOCHEM*, 1998, **425**, 155–159.
39 J. P. Paolini, The bond order—bond length relationship, *J. Comput. Chem.*, 1990, **11**, 1160–1163.
40 C. Adamo and V. Barone, Toward reliable density functional methods without adjustable parameters: the PBE0 model, *J. Chem. Phys.*, 1999, **110**, 6158–6170.
41 S. Grimme, J. Antony, S. Ehrlich and H. Krieg, A consistent and accurate ab initio parametrization of density functional dispersion correction (DFT-D) for the 94 elements H-Pu, *J. Chem. Phys.*, 2010, **132**, 154104.
42 S. Grimme, S. Ehrlich and L. Goerigk, Effect of the damping function in dispersion corrected density functional theory, *J. Comput. Chem.*, 2011, **32**, 1456–1465.
43 F. Weigend and R. Ahlrichs, Balanced basis sets of split valence, triple zeta valence and quadruple zeta valence quality for H to Rn: design and assessment of accuracy, *Phys. Chem. Chem. Phys.*, 2005, **7**, 3297–3305.
44 J. Tomasi, B. Mennucci and R. Cammi, Quantum mechanical continuum solvation models, *Chem. Rev.*, 2005, **105**, 2999–3094.
45 G. Scalmani, M. J. Frisch, B. Mennucci, J. Tomasi, R. Cammi and V. Barone, Geometries and properties of excited states in the gas phase and in solution: theory and application of a time-dependent density functional theory polarizable continuum model, *J. Chem. Phys.*, 2006, **124**, 094107.
46 M. J. Frisch, G. W. Trucks, H. B. Schlegel, G. E. Scuseria, M. A. Robb, J. R. Cheeseman, G. Scalmani, V. Barone and G. A. Petersson, *et al.*, *Gaussian 16 Rev. A.03*, Gaussian Inc., Wallingford CT, 2016.
47 H. Geng, Y. L. Niu, Q. Peng, Z. G. Shuai, V. Coropceanu and J.-L. Brédas, Theoretical study of substitution effects on molecular reorganization energy in organic semiconductors, *J. Chem. Phys.*, 2011, **135**, 104703.

48 Y. L. Niu, W. Q. Li, Q. Peng, H. Geng, Y. P. Yi, L. J. Wang, G. J. Nan, D. Wang and Z. G. Shuai, Molecular materials property prediction package (MOMAP) 1.0: a software package for predicting the luminescent properties and mobility of organic functional materials, *Mol. Phys.*, 2018, **116**, 1078–1090.
49 M. Isegawa, F. Neese and D. A. Pantazis, Ionization energies and aqueous redox potentials of organic molecules: comparison of DFT, correlated ab initio theory and pair natural orbital approaches, *J. Chem. Theory Comput.*, 2016, **12**, 2272–2284.
50 C. F. Wang, L. Q. Ouyang, X. F. Xu, S. Braun, X. J. Liu and M. Fahlman, Relationship of ionization potential and oxidation potential of organic semiconductor films used in photovoltaics, *Sol. RRL*, 2018, **2**, 1800122.
51 R. Kar, J. W. Song and K. Hirao, Long-range corrected functionals satisfy Koopmans' theorem: calculation of correlation and relaxation energies, *J. Comput. Chem.*, 2013, **34**, 958–964.
52 J.-L. Brédas, Mind the gap!, *Mater. Horiz.*, 2014, **1**, 17–19.
53 C.-K. Lin, M.-C. Li, M. Yamaki, M. Hayashi and S. H. Lin, A theoretical study on the spectroscopy and the radiative and non-radiative relaxation rate constants of the $S_0{}^1A_1$–$S_1{}^1A_2$ vibronic transitions of formaldehyde, *Phys. Chem. Chem. Phys.*, 2010, **12**, 11432–11444.
54 S. H. Lin, C. H. Chang, K. K. Liang, R. Chang, Y. J. Shiu, J. M. Zhang, T. S. Yang, M. Hayashi and F. C. Hsu, Ultrafast dynamics and spectroscopy of bacterial photosynthetic reaction centers, *Adv. Chem. Phys.*, 2002, 1–88.
55 W. L. Cai, A. C. Zhao, K. Ren, R. X. He, M. Li and W. Shen, Understanding the mechanisms of white light emission of a tetradentate Pt complex in various surrounding environments, *J. Phys. Chem. C*, 2019, **123**, 17968–17975.
56 F. C. Spano, The spectral signatures of Frenkel polarons in H-and J-aggregates, *Acc. Chem. Res.*, 2010, **43**, 429–439.
57 J. Gierschner, H.-G. Mack, H.-J. Egelhaaf, S. Schweizer, B. Doser and D. Oelkrug, Optical spectra of oligothiophenes: vibronic states, torsional motions, and solvent shifts, *Synth. Met.*, 2003, **138**, 311–315.
58 Y. L. Niu, Q. Peng, C. M. Deng, X. Gao and Z. G. Shuai, Theory of excited state decays and optical spectra: application to polyatomic molecules, *J. Phys. Chem. A*, 2010, **114**, 7817–7831.